J. Fluid Mech. (2016), *vol.* 798, *pp.* 572–597. © Cambridge University Press 2016
doi:10.1017/jfm.2016.321

Turbulent heat exchange between water and ice at an evolving ice–water interface

Eshwan Ramudu[1,†], Benjamin Henry Hirsh[1], Peter Olson[1] and Anand Gnanadesikan[1]

[1]Department of Earth and Planetary Sciences, Johns Hopkins University, Baltimore, MD 21218, USA

(Received 17 November 2015; revised 24 March 2016; accepted 4 May 2016;
first published online 7 June 2016)

We conduct laboratory experiments on the time evolution of an ice layer cooled from below and subjected to a turbulent shear flow of warm water from above. Our study is motivated by observations of warm water intrusion into the ocean cavity under Antarctic ice shelves, accelerating the melting of their basal surfaces. The strength of the applied turbulent shear flow in our experiments is represented in terms of its Reynolds number Re, which is varied over the range $2.0 \times 10^3 \leqslant Re \leqslant 1.0 \times 10^4$. Depending on the water temperature, partial transient melting of the ice occurs at the lower end of this range of Re and complete transient melting of the ice occurs at the higher end. Following these episodes of transient melting, the ice reforms at a rate that is independent of Re. We fit our experimental measurements of ice thickness and temperature to a one-dimensional model for the evolution of the ice thickness in which the turbulent heat transfer is parameterized in terms of the friction velocity of the shear flow. Applying our model to field measurements at a site under the Antarctic Pine Island Glacier ice shelf yields a predicted melt rate that exceeds present-day observations.

Key words: ocean processes, solidification/melting, turbulent boundary layers

1. Introduction

The exchange of heat and salt across the turbulent boundary layer at the ice–ocean interface governs the rate at which sea ice and ice shelves melt or grow in response to changes in ocean properties. Estimates of the heat exchange at such interfaces vary substantially across observational and modelling studies. In order to predict the evolution of sea ice and ice shelves more accurately, better constraints on their heat exchange with the underlying ocean are needed.

Antarctica is surrounded by ice shelves, thick floating sheets of ice that extend from the grounding line onto the ocean surface. They play a critical role in the mass balance and dynamics of Antarctica's terrestrial ice by serving as a buttress at the coastline and limiting the rate of ice flow into the ocean (Hooke 2005). Antarctic ice shelves are also important to the formation of Antarctic Bottom Water, a mass of dense water that fills approximately one half of the deep ocean (Broecker *et al.* 1998) and that plays an important role in the carbon cycle (Marinov *et al.* 2008).

† Email address for correspondence: eramudu@jhu.edu

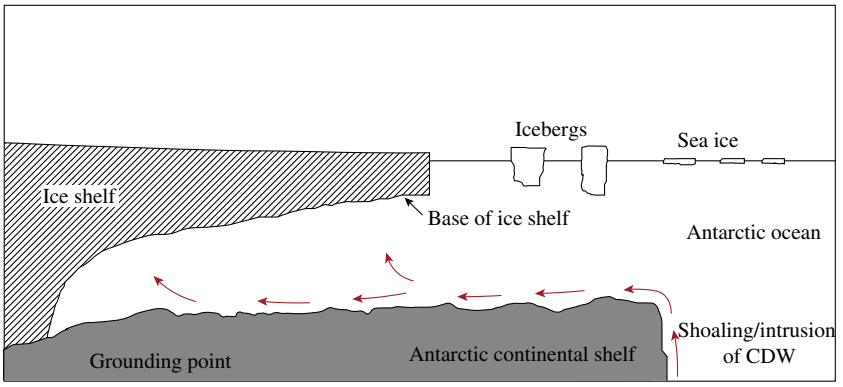

FIGURE 1. (Colour online) Warm Circumpolar Deep Water (CDW) rising into the ocean cavity under an Antarctic ice shelf.

Recent studies show that warm and salty Circumpolar Deep Water around Antarctica is shoaling onto the continental shelf and intruding into the ocean cavities under ice shelves, causing increased melting of their basal surfaces (Jacobs *et al.* 2011; Pritchard *et al.* 2012; Schmidtko *et al.* 2014). This process is depicted in figure 1. Increased basal melting can trigger the disintegration of ice shelves (Feldmann & Levermann 2015) and hence accelerate Antarctic ice loss, which would contribute significantly to global sea level rise. The rough topography of the ocean floor under ice shelves may play a role in guiding the warm shoaling water inside the cavity (Brisbourne *et al.* 2014). Basal melting results in a buoyant plume of meltwater that flows along the shelf base, generating turbulence, which in turn affects both the transfer of heat to the shelf and the entrainment of heat from the relatively warm far field into the relatively cold boundary layer (Little, Gnanadesikan & Hallberg 2008).

Previous studies of ice shelf–ocean interaction have been conducted mainly through numerical models. The heat transfer from the ocean mixed layer to the ice shelf base in these models is parameterized in terms of the temperature difference across, and the thermal exchange velocity γ_T through, the boundary layer. γ_T is defined as the ratio of the thermal diffusivity to the thickness of the boundary layer. In the earlier works of Hellmer & Olbers (1989) and Scheduikat & Olbers (1990), γ_T was taken to be a constant. Jenkins (1991) followed the theory of Kader & Yaglom (1972), assuming that the ice–water interface is hydraulically smooth, and expressed γ_T in terms of the friction velocity of the turbulent boundary layer. This formulation was used in the studies by Holland & Feltham (2006) and Jenkins, Nicholls & Corr (2010*b*). McPhee, Maykut & Morison (1987) developed a parameterization for γ_T by using the formulation of Yaglom & Kader (1974) for the transfer of heat in a turbulent boundary layer near a rough wall and by additionally considering the effect of buoyancy and rotation on heat transfer. Holland & Jenkins (1999), Mueller *et al.* (2012) and Dansereau, Heimbach & Losch (2014) adopted this parameterization in their studies. The formation of channels in the ice shelf base as a result of plumes flowing on the underside of the shelf has also been investigated numerically (Dallaston, Hewitt & Wells 2015).

There are numerous laboratory experiments on heat transfer at a phase change boundary between a solid and a liquid that are relevant to our study. Townsend (1964) investigated the evolution of the layer of free convection over an ice surface

into a stable liquid layer above. The instability of an ice surface, and subsequent formation of a wavy interface, in the presence of a turbulent flow was explored by Gilpin, Hirata & Cheng (1980). Significant work has been performed on the study of the formation of a mushy layer and on compositional and thermal convection in the liquid during the solidification of a binary solution to explain brine rejection as sea ice forms (Huppert & Worster 1985; Wettlaufer, Worster & Huppert 1997). The effect of an external shear flow on a mushy layer has also been investigated (Neufeld & Wettlaufer 2008). In the latter study, a laminar shear flow was applied to an NH_4Cl mushy layer from above and the primary focus was the stability of the mushy layer in response to the shear flow. Kerr & McConnochie (2015) developed a theoretical model for the dissolution of a vertical solid surface and tested their model with experimental measurements. These laboratory studies provide an explanation of the physical processes at an ice–water interface and are useful guides for investigating the effect of turbulent warm water at an ice–ocean interface. Also related to ice shelf–ocean interaction is the set of experiments by Stern *et al.* (2014) on the effect of geometry on circulation inside the ice shelf cavity and at the ice shelf front. None of these studies, however, consider the effect of shear-driven turbulence on what is essentially a horizontal ice shelf–ocean interface.

In this paper, we describe an experimental study on the response of an ice–water interface to forced convection in the form of turbulent mixing in pure water over ice. The experiments are conducted in a cylindrical tank with a layer of ice growing on a basal cooling plate at the bottom, representing the base of an ice shelf. The overlying water layer is covered at the top by a lid with a rough underside. This rough surface drives the motion in the water column and creates a well-mixed turbulent liquid layer when the lid is rotated. Turbulent mixing causes warm water to be transported from the far field to the ice–water interface. Our laboratory set-up is an idealized, inverted model of the ocean cavity under Antarctic ice shelves in which the circulation of relatively warm water is reaching the basal surface of these ice shelves, causing accelerated basal melting. The set-up is inverted because the boundary layer at the ice–water interface in the experiments is denser than the far field, whereas in the ocean, the boundary layer is relatively buoyant. There is no natural convection in our experiments and hence the boundary layer is stable in the absence of turbulent mixing.

An important difference between the laboratory set-up and the oceanographic case is the absence of salt in the experiments. The ice–ocean interface is at a temperature intermediate between the salinity-dependent freezing point of the ocean and the melting point of ice in fresh water (0 °C). The rate of phase change at the ice–ocean interface is governed by both the conservation of heat and the conservation of salt at the interface. When there is a large heat flux through the boundary layer to the ice–ocean interface, melting occurs. When the liquid far-field temperature is below the melting point of ice at the interface and the interface salinity is non-zero, conservation of salt at the interface causes ice to dissolve (Wells & Worster 2011; Kerr & McConnochie 2015). In this experimental study, we ignore the effect of salinity on the interface temperature, and we focus uniquely on the phase change due to heat transfer, melting.

We formulate a theoretical model for the evolution of the ice thickness in our experiments and compare our measurements with the prediction from our theoretical model in order to develop a parameterization for the turbulent heat transfer at the ice–water interface. The apparatus and procedure are described in § 2. In § 3, the governing equations in our theoretical model are outlined. The results from the set

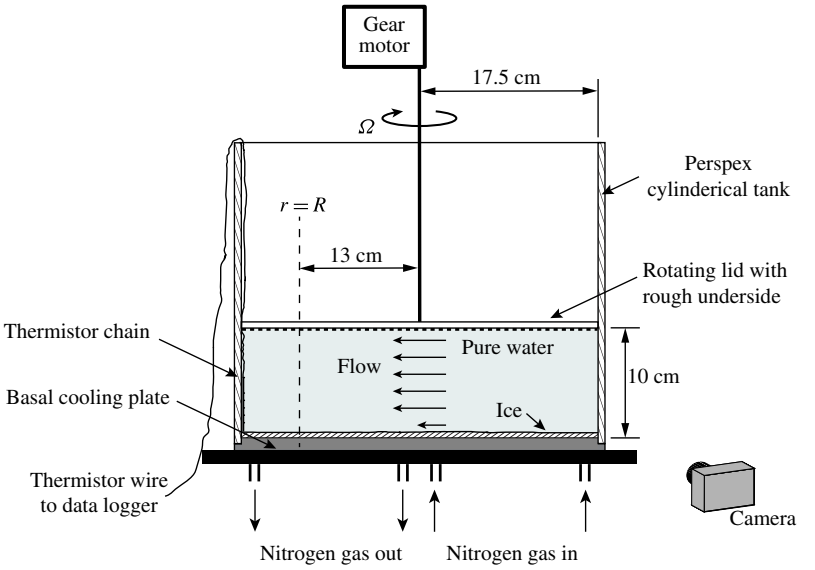

FIGURE 2. Schematic diagram of the apparatus.

Non-dimensional number	Definition	Experiment	Ice shelf cavity
Reynolds, *Re*	UD/ν	10^3–10^4	10^6
Friction Reynolds, Re_*	u_*D/ν	10^2–10^3	10^5
Rossby, *Ro*	$U/\Omega D$	0.7	1
Stefan, *St*	$c_s\Delta T_s/L$	0.2	0.2
Prandtl, *Pr*	ν/α_ℓ	13.6	13.8
Péclet, *Pe*	UD/α_ℓ	10^4–10^5	10^7
Volumetric heat capacity ratio, $\mathscr{C}$	$\rho_\ell c_\ell/\rho_s c_s$	2.2	2.2
Thermal diffusivity ratio, *A*	α_ℓ/α_s	0.12	0.12

TABLE 1. Dimensionless control parameters in the experiment and in an ice shelf cavity.

of experiments are shown in § 4 and are compared to the theoretical model in § 5. In § 6, we discuss the geophysical application of our results. Finally, we summarize our study in § 7.

The dimensionless control parameters that are relevant to the study are the Reynolds number, friction Reynolds number, Rossby number and Stefan number. The definition of these parameters and their estimated values in our experiments and in an ice shelf cavity are listed in table 1. In the definitions, the subscript s refers to the solid (ice) and the subscript ℓ refers to the liquid (water). D denotes the depth of the liquid layer; U, the characteristic velocity scale; u_*, the friction velocity; ν, the kinematic viscosity; Ω, the angular frequency of rotation; ρ, the density; c, the specific heat capacity; ΔT, the temperature difference; L, the specific latent heat; and α, the thermal diffusivity.

2. Experimental method

The experimental apparatus is shown in figure 2. It consists of a cylindrical tank of radius 17.5 cm with 1.5 cm thick Perspex walls and a 5 cm thick aluminium basal

Property	Units	Liquid water	Solid ice
Freezing temperature, T_f	K		273.15[b]
Density, ρ	kg m^{-3}	999.8[a]	916.7 [b]
Specific latent heat of fusion, L	J kg^{-1}		3.33×10^5 [b]
Isobaric specific heat capacity, c	J kg^{-1} K^{-1}	4.21×10^3 [a]	2.10×10^3 [b]
Thermal conductivity, k	W m^{-1} K^{-1}	0.556[b]	2.16[b]
Kinematic viscosity, μ	Pa s	1.79×10^{-3} [b]	
Thermal expansion coefficient, β	K^{-1}	6.77×10^{-5} [c]	160 [b]

TABLE 2. Physical properties of liquid water and ice at standard atmospheric pressure. ρ, L, c, k, μ and β at 273.15 K. β for liquid water is linear and β for solid ice is volumetric. [a]From Wagner & Pruß (2002), [b]from Haynes (2015) and [c]from IOC, SCOR & IAPSO (2010).

cooling plate. The tank is filled with pure water to a height of 10 cm, and ice is grown by circulating cold nitrogen gas inside the basal cooling plate. The physical properties of liquid water and ice are listed in table 2. The interior of the plate consists of two sets of parallel spiral grooves, one set having an inlet at the centre and an outlet near the rim and the other set having an inlet near the rim and an outlet at the centre. This arrangement helps achieve a uniform heat flux through the plate and hence uniform ice growth on its surface. The nitrogen flow rate is held constant at 0.14 m^3 min^{-1} within and across experiments. A Perspex cover lid is positioned at the upper surface of the water layer, connected to a gear motor by means of a vertical metal rod. A plastic grid is attached to the underside of the cover lid, creating a rough surface for generating the turbulent shear flow. The grid consists of a lattice of squares, each square having sides of length 1.4 cm and projecting downward beneath the lid a distance of 0.9 cm. The rotation of the cover lid and plastic grid is controlled by the gear motor.

To start each experiment, the water layer, initially at rest and at room temperature, is suddenly cooled from below by turning on the flow of nitrogen into the basal cooling plate. It typically takes approximately 30 min for ice to begin to nucleate on the basal plate. The ice is allowed to grow for another 30 min, reaching a nearly uniform thickness of 8–12 mm, depending on the initial temperature of the water. The motor is then turned on, rotating the lid and grid at a constant angular velocity, typically for approximately one hour. We experimented with lid angular velocities between 0.27 and 1.43 rad s^{-1}, fast enough to generate a turbulent shear flow that extends to within approximately 1.5 cm of the bottom surface of the tank in each case.

Pictures of the ice are taken from the side of the tank at 1 min intervals with a Nikon D800 camera. The ice thickness is subsequently measured from these pictures using GraphClick, a digitizer software. Seven thermistors are placed on a 5.25 cm long vertical strip starting from the bottom of the tank to measure temperature at the locations shown in figure 3. The strip is placed along the wall of the tank and the thermistors protrude 1 cm into the tank. The thermistors are connected to a data logger. We focus on the ice thickness at a radial distance $R = 13$ cm from the tank centre, that is, 4.5 cm from the outer wall. This location is a compromise between its proximity to the thermistor chain and its separation from the immediate effects of the outer wall.

Both the friction velocity and fluid velocity of the turbulent shear flow are measured over the entire range of lid angular velocities. The average shear stress, and hence friction velocity, is obtained by measuring the torque on the lid with a torque

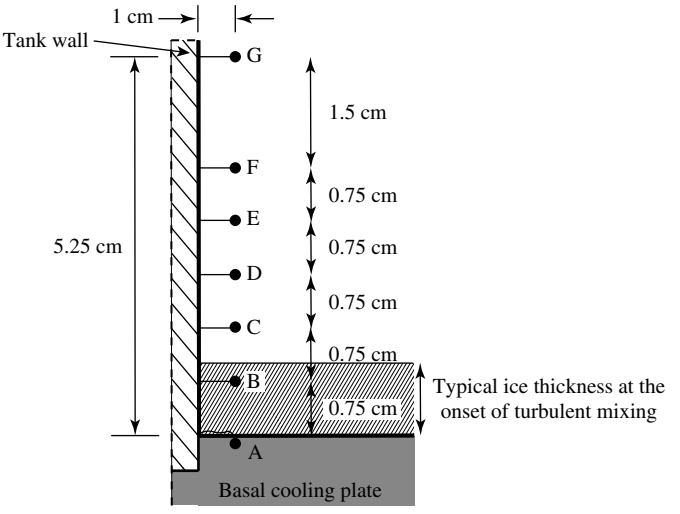

FIGURE 3. Arrangement of thermistors.

meter. The fluid velocity is obtained from planar particle image velocimetry (PIV) measurements. The water is seeded with nearly spherical glass beads of specific gravity 1.1 and average diameter 10 μm and illuminated with a pulsed Nd:YAG laser sheet. A vertical light sheet is set up along a chord at $r = R$ to measure the vertical profile of the azimuthal component of the velocity. To measure the radial component of the velocity, a horizontal light sheet is set up to illuminate a sector of the tank's circular cross-sectional area at different heights above the bottom plate. A high-speed CMOS camera synchronized with the pulsed laser taking double exposure images at a resolution of 2048×2048 pixels is oriented vertically above the tank and horizontally to the side of the tank, for imaging the radial flow and azimuthal flow, respectively. The open source software PIVlab (Thielicke & Stamhuis 2014) is used to calculate PIV velocities from the exposures. For the determinations of the azimuthal velocity profiles, only a vertical strip at the centre of the images taken from the side, in which the particles move in the plane of the light sheet, is used in the analysis.

3. Ice energy balance

The energy (enthalpy) balance in a control volume enclosing the ice with thickness h at a time t shown in figure 4 yields the following relationship:

$$\frac{\mathrm{d}E}{\mathrm{d}t} = Q_p + Q_\ell, \tag{3.1}$$

where E is the energy (enthalpy) content of the ice, the subscript p refers to the plate and Q is the heat entering the control volume from the region denoted by its subscript. Considering a one-dimensional energy balance, E and Q_p can be expressed as

$$E = \rho_s c_s \int_0^h \overline{T_s}\,\mathrm{d}z - \rho_s L h \tag{3.2}$$

and

$$Q_p = -\frac{k_s \Delta T_s}{h}. \tag{3.3}$$

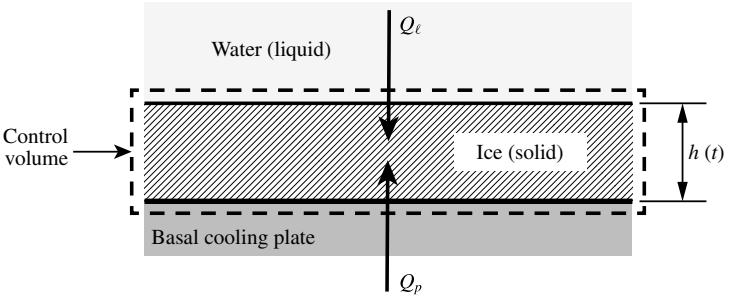

FIGURE 4. Control volume around ice.

In (3.2) and (3.3), k is thermal conductivity and T is temperature. $\Delta T_s = T_f - T_p$, where T_f is the freezing temperature of water (also the temperature of the ice–water interface). $\overline{T_s}$ is the average temperature of the ice. Assuming that the temperature varies linearly in the vertical direction through the ice, $\overline{T_s} = (T_f + T_p)/2$. Numerical values of the physical properties of water and ice are given in table 2. The first term on the right-hand side in (3.2) can be rewritten as

$$\rho_s c_s \int_0^h \overline{T_s}\,\mathrm{d}z = \rho_s c_s h \left(\frac{\Delta T_s}{2} + T_p\right). \tag{3.4}$$

3.1. *No turbulent mixing*

When the ice is growing in quiescent water, heat is transferred by conduction. We ignore free convection in the liquid. In this case Q_ℓ is the sum of the conductive heat transfer through and the rate of change of enthalpy of the liquid, so that

$$Q_\ell = \frac{k_\ell \Delta T_\ell}{\delta} + \rho_s c_s T_f \frac{\mathrm{d}h}{\mathrm{d}t}, \tag{3.5}$$

where the subscript ℓ refers to the liquid properties, δ is the thickness of the thermal boundary layer above the ice and $\Delta T_\ell = T_\infty - T_f$, T_∞ being the temperature of the liquid far field. Introducing

$$\delta = \frac{\alpha_\ell}{\mathrm{d}h/\mathrm{d}t} \tag{3.6}$$

from the heat balance in a control volume in the liquid region above the ice–water interface, with α_ℓ given by

$$\alpha_\ell = \frac{k_\ell}{\rho_\ell c_\ell}, \tag{3.7}$$

the conductive term in (3.5) can be rewritten as

$$\frac{k_\ell \Delta T_\ell}{\delta} = \rho_\ell c_\ell \Delta T_\ell \frac{\mathrm{d}h}{\mathrm{d}t}. \tag{3.8}$$

Substitution of (3.2)–(3.5), and (3.8) into (3.1) gives, for the heat balance in the control volume,

$$\left(\rho_s L + \frac{\rho_s c_s \Delta T_s}{2} + \rho_\ell c_\ell \Delta T_\ell\right) \frac{\mathrm{d}h}{\mathrm{d}t} = \frac{k_s \Delta T_s}{h} + \frac{\rho_s c_s h}{2} \frac{\mathrm{d}}{\mathrm{d}t}(\Delta T_s), \tag{3.9}$$

which can be approximated, based on the largest terms, as

$$(\rho_s L + \rho_\ell c_\ell \Delta T_\ell)\frac{\mathrm{d}h}{\mathrm{d}t} \simeq \frac{k_s \Delta T_s}{h}. \tag{3.10}$$

This equation is non-dimensionalized by taking the length scale to be the depth D of the liquid, the temperature difference scale to be the temperature difference across the solid at the onset of turbulent mixing and the time scale to be D^2/α_ℓ, which corresponds to the characteristic time for thermal diffusion over the distance D. This yields

$$\left[\frac{1}{St} + \mathscr{C}(\Delta T_\ell)^*\right]\frac{\mathrm{d}h^*}{\mathrm{d}t^*} = \frac{1}{A}\frac{(\Delta T_s)^*}{h^*}, \tag{3.11}$$

where variables with a superscript $*$ are in non-dimensional form. $\mathscr{C} = \rho_\ell c_\ell/\rho_s c_s$ is the ratio of the volumetric heat capacity of the liquid to that of the solid and $A = \alpha_\ell/\alpha_s$ is the ratio of the thermal diffusivity of the solid to that of the liquid. The typical values of $\mathscr{C}$ and A for the laboratory experiment and for the geophysical application are listed in table 1.

3.2. *Turbulent mixing*

For turbulent flow over a flat plate at constant temperature, Reynolds analogy relates the convective heat flux q_T to the properties of the momentum boundary layer. In Reynolds analogy, the heat flux and momentum flux at the plate in a turbulent boundary layer are considered equivalent since they are both influenced by the turbulent motion above the plate. The expression for q_T (see White 1974, p. 564) is

$$q_T = \rho_\ell U_\infty c_\ell \Delta T_\ell C_h, \tag{3.12}$$

where C_h is a heat transfer coefficient (Stanton number) given empirically by

$$C_h = \frac{c_f/2}{1 + 12.8(Pr^{0.68} - 1)\sqrt{c_f/2}}, \tag{3.13}$$

U_∞ is the velocity of the liquid in the far field, Pr is the Prandtl number and c_f is the coefficient of friction defined as

$$c_f = 2\frac{u_*^2}{U_\infty^2}, \tag{3.14}$$

where u_* is the friction velocity. We introduce the coefficient G in the expression for C_h to substitute for the constant term $12.8(Pr^{0.68} - 1)$. In the context of our experiment, this term is the term we are trying to constrain. For the turbulent mixing phase in our experiments, Q_ℓ is augmented by q_T, and hence the energy balance for the control volume becomes

$$(\rho_s L + \rho_\ell c_\ell \Delta T_\ell)\frac{\mathrm{d}h}{\mathrm{d}t} \simeq \frac{k_s \Delta T_s}{h} - \rho_\ell U_\infty c_\ell \Delta T_\ell C_h. \tag{3.15}$$

By using the same length, temperature difference and time scales as in (3.11) and by additionally using U_∞ as the velocity scale, this expression is non-dimensionalized to obtain

$$\left[\frac{1}{St} + \mathscr{C}(\Delta T_\ell)^*\right]\frac{\mathrm{d}h^*}{\mathrm{d}t^*} = \frac{1}{A}\frac{(\Delta T_s)^*}{h^*} - RePr\mathscr{C}(\Delta T_\ell)^* C_h, \tag{3.16}$$

where $RePr = Pe$. Table 1 lists typical values of Pe for the sub-ice shelf cavity and the laboratory set-up.

Experiment	Ω (rad s^{-1})	Lid Re_R	Regime
0	0	0	
1	0.27	2.0×10^3	Attenuated growth
2	0.32	2.3×10^3	Partial melting
3	0.45	3.3×10^3	Partial melting
4	0.60	4.4×10^3	Partial melting
5	0.71	5.2×10^3	Partial melting
6	0.82	5.9×10^3	Complete melting
7	0.98	7.1×10^3	Complete melting
8	1.14	8.3×10^3	Complete melting
9	1.31	9.5×10^3	Complete melting
10	1.43	1.0×10^4	Complete melting

TABLE 3. Angular frequency Ω of lid and lid Re_R in experiments.

4. Experimental results

We conducted a set of eleven experiments at different angular velocities of rotation Ω of the lid. The value of Ω for each experiment is listed in table 3. Experiment 0 is a null experiment in which the lid was not rotated, and hence the water was not mixed by turbulence over the whole duration. The lid Re at a radius r, Re_r, in the tank is defined as

$$Re_r = \frac{(\Omega r)D}{\nu}. \tag{4.1}$$

When Ωr is taken as the velocity scale U, this definition of Re is the same as in table 1. The value of Re_r at $r = R$, which we denote by Re_R, for each experiment is given in table 3. We refer to the first portion of each experiment in which ice grows by conduction in still water as Phase 1 and the second portion of each experiment in which there is a turbulent shear flow and mixing as Phase 2.

We conducted a separate test to estimate the heat flux through the tank wall during Phase 2 of a typical experiment. A set of thermistors was placed on the external surface of the tank to measure its temperature, which was used to estimate the temperature difference across the tank wall. At the end of the turbulent mixing phase of the experiment, when the liquid inside the tank is coldest, the heat flux through the tank wall is approximately 3 % of the turbulent heat flux from the liquid to the ice–water interface in the interior of the tank.

4.1. *Ice thickness*

Measured ice thickness h_e versus time is shown in figures 5 and 6, from experiments 1–10 and experiment 0 respectively. In figure 5 the time $t = 0$ corresponds to the onset of the turbulent shear flow. In figure 6, the shaded region along the line plot has a total width of 0.5 mm and represents the error in the measurements. The error was estimated by taking the standard deviation of 10 repeated measurements of the ice thickness at $r = R$ during Phase 1 of a typical experiment. The ice thickness measurements in experiment 0 and in Phase 1 of experiments 1–10 are assigned the same error estimate.

The error in Phase 2 measured by the same method, using Phase 2 measurements from a typical experiment, is 0.9 mm. The error in ice thickness measurements in

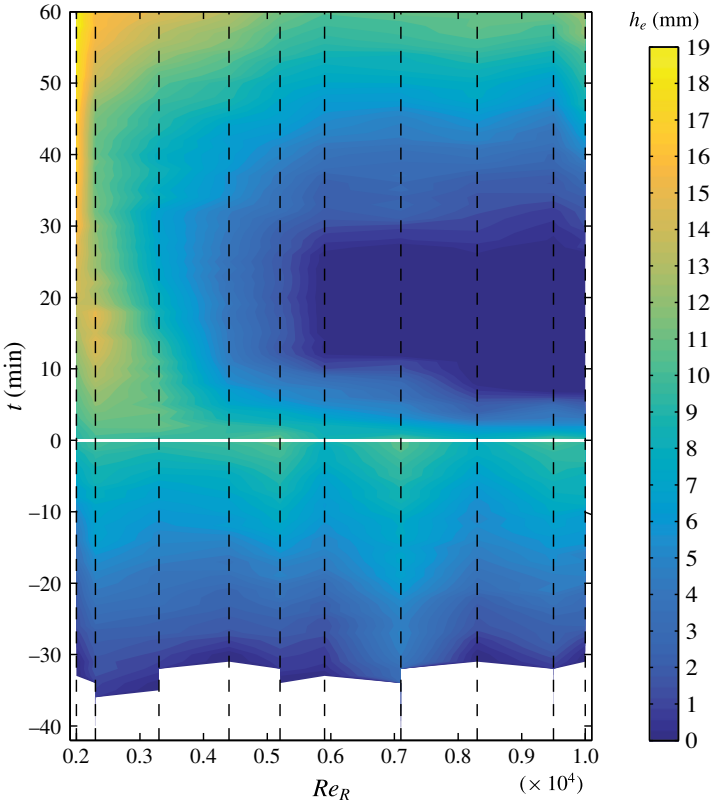

FIGURE 5. (Colour online) Ice thickness at $r = R$ over the course of experiments 1–10. The vertical axis denotes the time relative to the onset of turbulent mixing in each experiment. The horizontal white line indicates the onset of mixing and dashed vertical black lines indicate the Re_R of each experiment. The contour plot has been constructed by linearly interpolating measurements from the 10 distinct experiments.

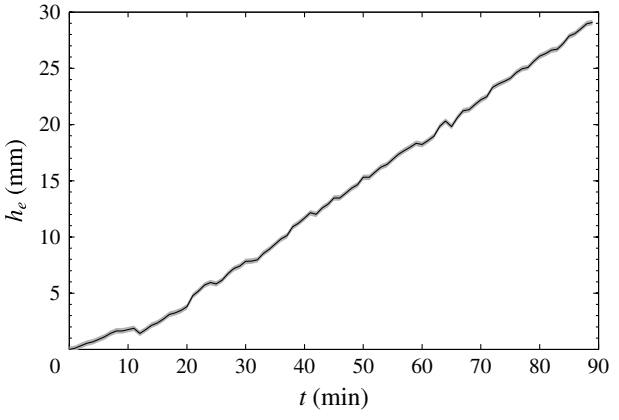

FIGURE 6. Ice growth in experiment 0 (with no shear flow).

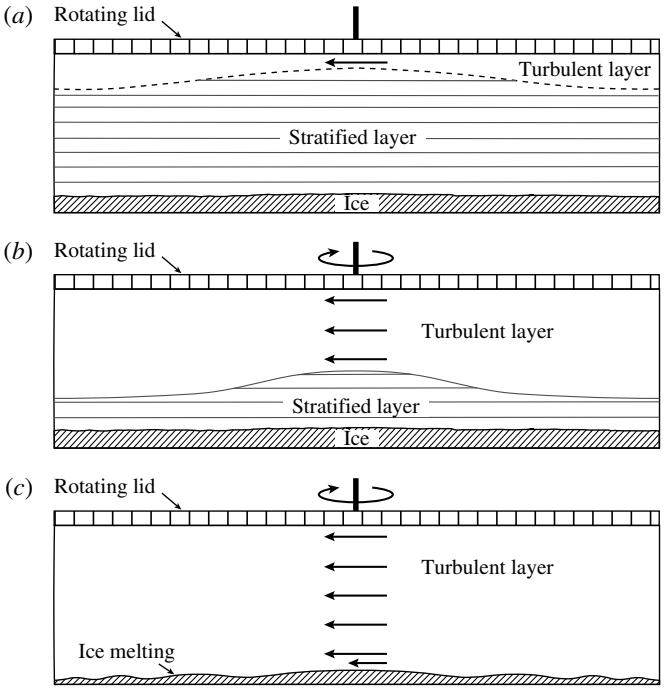

FIGURE 7. Changes in the liquid layer following the onset of turbulent mixing. At the lower end of experimental Re_R, the steps shown in this diagram occur over several minutes, whereas at the upper end of experimental Re_R, they occur in a few seconds. (*a*) A stratified layer initially separates the turbulent layer from the ice surface. The interface between the stratified layer and turbulent layer is dome shaped. (*b*) The turbulent layer progresses downwards, eroding the stratified layer. (*c*) The turbulent layer has reached the ice–water interface and causes the ice to melt. The thickness of ice melted increases with radius. A spiral wavy profile develops on the ice surface during melting.

Phase 2 is larger than in Phase 1 because the ice–water interface becomes wavy when ice melts in the presence of the turbulent flow. The wavy pattern consists of spiral crests and troughs with wavelength 12–16 mm and amplitude 1–3 mm. It is difficult to visually identify the ice thickness along the diameter from the side-view pictures of the tank due to the waviness of the ice surface.

Ice grows at an almost constant rate when the water is undisturbed, as in experiment 0 and in Phase 1 of experiments 1–10. In Phase 2, mixing by the turbulent shear flow transports warm water from the far field to the ice–water interface, which promotes heat transfer to the ice. The ice then responds in one of three ways, each of which we have observed as a transient at our measurement location $r = R$: (1) attenuated ice growth, (2) partial melting and (3) complete melting. Attenuated growth refers to ice growing at a rate slower than during Phase 1. Partial melting refers to only a fraction of the ice thickness from Phase 1 changing phase into liquid, such that a residual thinner ice layer still remains in the tank. Complete melting refers to the whole ice layer from Phase 1 changing phase into liquid. Following this transient response, regrowth of ice at the same rate as in Phase 1 is observed.

Figure 7 shows the sequence of structures that are observed in the ice–water system following the onset of turbulent mixing. A thermally stratified water layer

initially separates the growing ice from the turbulent flow, as the turbulence develops beneath the rotating lid. The interface between the stratified layer and the turbulent flow is dome shaped because the turbulent shear stress τ increases proportionally to r^2 and is therefore weaker near the centre of the tank. The dome-shaped interface was imaged in the experiments by inserting dye at the top of the water column into the turbulent layer and monitoring the evolution of the turbulent layer. In our lowest Re_R experiment, the stratified layer persists in the presence of the shear flow, thereby preventing turbulence from reaching the ice–water interface. Ice growth is attenuated in this case, but not stopped. At the other extreme, in our highest Re_R experiments, the turbulent mixing is strong enough to erode the stratified layer entirely almost immediately after the onset of the turbulent shear flow. When the turbulence comes in direct contact with the ice–water interface, it produces complete melting at high Re_R and partial melting at intermediate Re_R. In the partial melting cases, the thickness of ice melted increases with radial distance from the tank centre. In table 3, the transient behaviour the ice adopts at $r = R$ in response to turbulent mixing in experiments 1–10 is given along with the corresponding Re_R.

The development of the spiral wavy pattern on the ice–water interface when ice melts in our experiments has been explained by Gilpin *et al.* (1980), as follows. Although the ice thickness is approximately uniform at the end of Phase 1, there are nevertheless small-amplitude deviations from uniform thickness due to random perturbations and minor design flaws in the cooling apparatus. Gilpin *et al.* (1980) found that such an interface will be unstable to growth in the presence of turbulence when the heat flux from the liquid to the solid is large, which is the case in our experiments during transient melting. The mechanism for the instability involves flow separation downstream of an irregularity in the ice, which causes the heat transfer at a crest to be smaller than the heat transfer at a valley. The amplitude of the irregularity thus grows, which further amplifies the irregularity in the shear flow, producing a growing set of undulations on the ice–water interface as it melts. The wavelength of the undulations increases with u_*, which is proportional to r in our experiments. The dependence of the undulation wavelength on distance from the tank centre gives rise to the spiral profile of the ice–water interface undulations that we observe.

4.2. *Temperature*

Thermistors A–G are used to measure the temperature at the heights indicated in figure 3. The resistance $\mathscr{R}$ of a thermistor is related to its temperature T according to the Steinhart–Hart equation,

$$\frac{1}{T} = a_1 + a_2 \ln \mathscr{R} + a_3 (\ln \mathscr{R})^3, \tag{4.2}$$

where a_1, a_2 and a_3 are the Steinhart–Hart coefficients and are unique to each thermistor. We obtained these coefficients by calibration prior to our series of experiments.

Temperature is recorded starting from the instant nitrogen starts to circulate inside the basal cooling plate. The evolution of temperature at the thermistor locations A–G in a typical experiment (in this case, experiment 6) is shown in figure 8. Occasional outliers in the thermistor readings have been deleted and the data points have been replaced by interpolating neighbouring values. These outliers are due to the thermistor connections occasionally freezing, causing sudden resistance increases which are seen as sudden temperature drops. Following the onset of turbulent mixing, there is an

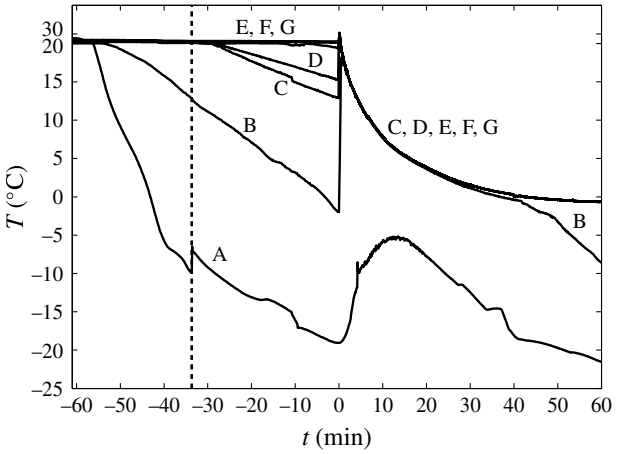

FIGURE 8. Temperature recorded by thermistors A, B, C, D, E, F and G over the course of a typical experiment. The horizontal axis denotes time relative to the onset of turbulent mixing. The vertical dashed line indicates the time at which ice forms a thin layer on the bottom plate.

increase in temperature at A because warm water transported to the bottom of the tank causes melting of ice. At that time, thermistors B, C, D, E, F and G record the same temperature, signalling that mixing results in a homogeneous distribution of temperature in the turbulent shear flow. Note that after about 40 minutes of cooling, the temperature at B departs from the temperatures at C, D, E, F and G as thermistor B is engulfed by the growing ice.

Vertical profiles of temperature in the same experiment at the indicated times during Phase 1 and Phase 2 are shown in figure 9(*a*,*b*) respectively. Because the ice–water interface is at $T_f = 0\,^{\circ}\mathrm{C}$, the measured ice thickness at any time can be checked by interpolating T_f in the temperature time series recorded by thermistors A–G. The temperature within the ice can safely be assumed to increase linearly from the temperature of the plate to T_f, because heat transfer in the ice is by conduction and its growth rate is slow enough that the ice is in thermal equilibrium with its boundaries. The linear distributions of ice temperature are shown by the straight lines in the left half of figure 9(*a*,*b*). Temperature profiles above the ice–water interface in Phase 1 (figure 9*a*) are exponential fits to the temperature measurements. For clarity, the temperature data points corresponding to only one profile have been included in each figure. The fitted liquid layer temperature profiles in Phase 1 are characteristic of heat transfer in the liquid by conduction only.

We saw no evidence of natural convection in the liquid layer during Phase 1. For a liquid water layer over an ice–water interface at 0 °C, natural convection onsets at Rayleigh numbers above 1700, which has been confirmed experimentally by Boger & Westwater (1967). The Rayleigh number for this system can be expressed as

$$\mathrm{Rayleigh} = \frac{d^3 \beta \rho_\ell^2 g c_\ell (\Delta T)}{\mu k_\ell}, \tag{4.3}$$

where β is the thermal expansion coefficient of water, d is the convecting layer depth and ΔT is the temperature difference across d. Boger & Westwater (1967) take d to

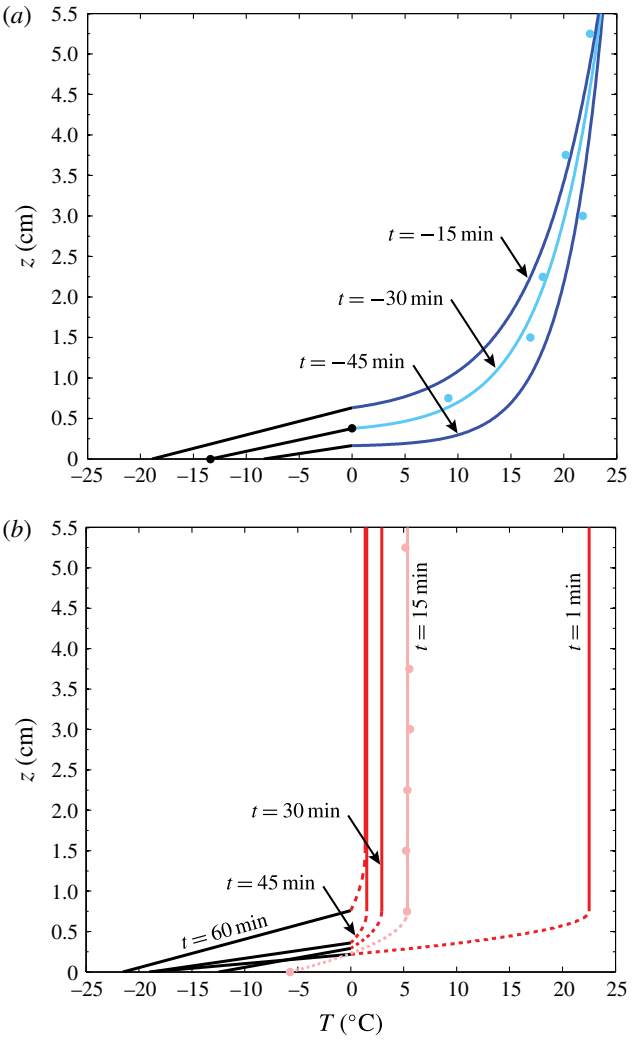

FIGURE 9. (Colour online) Vertical profiles of temperature at different times relative to the onset of turbulent mixing during (*a*) Phase 1 and (*b*) Phase 2 of a typical experiment. The temperature data points are shown for the $t = -30$ min profile in (*a*) and for the $t =$ 15 min profile in (*b*). In (*b*), a dashed line is drawn between the location of the ice–water interface and the location of the first thermistor above the ice–water interface to indicate a possible temperature profile in that layer. Liquid temperature profiles in Phase 1 are in blue and liquid temperature profiles in Phase 2 are in red.

be the thickness of the liquid layer between the ice–water interface and the height at which the water is at 4 °C, where it has maximum density. Interpolating the value of d from the temperature measurements in Phase 1 of our experiments and using values from table 2 for the physical properties of water, we found that the Rayleigh number in Phase 1 varies from 250 to approximately 850. It therefore remains below the critical Rayleigh number at which natural convection would occur.

As the liquid cools by conduction in Phase 1 of an experiment, the temperature T in its thermal boundary layer can be modelled according to the relation

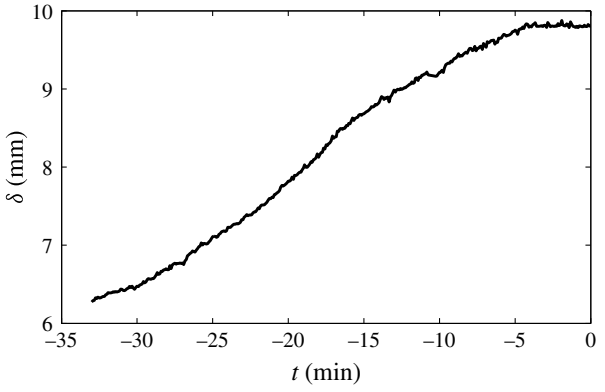

FIGURE 10. Boundary layer thickness δ calculated from exponential fit through non-dimensionalized vertical temperature time series.

$$\frac{T - T_f}{T_\infty - T_f} = 1 - \mathrm{e}^{-(z-h_e)/\delta}, \quad z \geqslant h_e. \tag{4.4}$$

The thickness δ of the thermal boundary layer can be obtained by taking the reciprocal of the fit coefficient of an exponential fit to this relationship. Figure 10 shows the evolution of δ calculated in this way in Phase 1 of the same experiment. The initial value of δ is non-zero because, prior to the formation of ice, a thermal boundary layer was already present in the liquid due to cooling from the bottom by the basal cooling plate. The thickness of the thermal boundary layer increases from its initial value as Phase 1 of the experiment proceeds. This indicates that, for a control volume in the liquid above the ice–water interface, the heat loss by conduction to the ice is larger than the enthalpy decrease of the control volume due to the movement of the ice–water interface into it. At the end of Phase 1, δ asymptotes to a uniform value. At this stage, the energy balance in the control volume above the ice–water interface is at steady state, that is, conductive heat loss to the ice is balanced by enthalpy decrease due to the upward movement of the ice–water interface. A simple one-dimensional model for the energy balance in the control volume gives $\delta = \alpha_\ell/(\mathrm{d}h_e/\mathrm{d}t)$. The predicted value of δ from this model for our case is 20 mm, which is approximately twice as large as the steady-state value of δ from figure 10. The rate of growth of ice, $\mathrm{d}h_e/\mathrm{d}t$, is very small in our experiment (about 5.5×10^{-3} mm s^{-1}). There is very little liquid convective motion in the control volume above the ice–water interface in response to the very slowly moving interface, and hence the thermal boundary layer is thinner than the theoretical prediction.

During Phase 2 of these experiments, all of the thermistors in the liquid typically record nearly the same temperature at a given time after the initial thermal stratification in the liquid has been destroyed by turbulent mixing. A vertical line through the mean of the temperatures measured by the thermistors in the liquid is drawn in figure 9(*b*) to represent a homogeneous vertical temperature profile in the liquid layer.

4.3. *Velocity*

Application of the heat balance shown in (3.15) to the control volume around the ice–water interface in figure 4 requires knowledge of the fluid velocity in the far field.

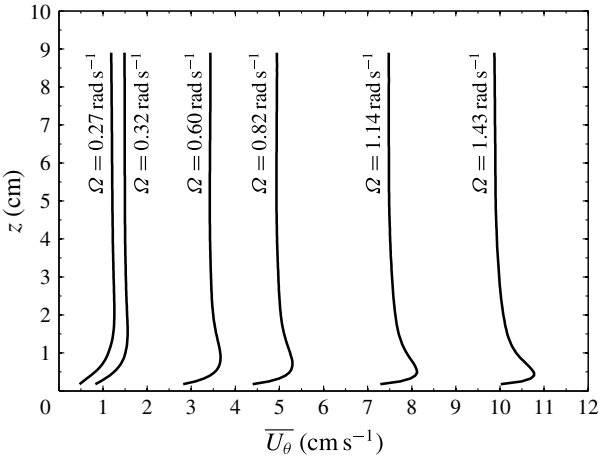

FIGURE 11. Mean azimuthal velocity in the fluid column at $r = R$ for different angular velocities of the lid.

Since the temperature distribution in the liquid is nearly homogeneous when there is turbulent mixing, buoyancy forces in the liquid are weak during this phase of the experiments. The circulation in the far field is thus due to the shear induced by the rotating lid only.

The velocity of the shear-driven turbulent flow above the flat bottom surface of the tank is measured for the purpose of relating the fluid velocity in the far field to the lid velocity. We denote by $\overline{U_\theta}$ the mean of the azimuthal velocity component and by $\overline{U_r}$ the mean of the radial velocity component of the flow. The vertical profiles of $\overline{U_\theta}$ corresponding to different lid angular velocities are shown in figure 11. They were obtained by horizontally averaging the horizontal component of the velocity vectors from PIV measurements in a vertical strip at $r = R$. Figure 12 shows $\overline{U_r}$ at different radial distances, including $r = R$, at a height of 0.5 and 7 cm above the basal cooling plate. The radial component of the velocity vectors from PIV measurements in a horizontal sector at these heights were averaged to obtain these profiles of $\overline{U_r}$.

The $\overline{U_\theta}$ plots show the presence of a thin boundary layer near the bottom plate. For higher angular frequencies of rotation Ω of the lid, $\overline{U_\theta}$ has a maximum within the boundary layer. We interpret this maximum to be due to the transfer of angular momentum from the flow near the wall along the bottom plate to the flow in the interior of the tank along the bottom plate. Above the boundary layer, there is a core region with uniform $\overline{U_\theta}$ that extends almost to the top of the fluid column. This uniform core can therefore be considered to be in solid body rotation. The velocity in the thin boundary layer near the rough underside surface of the lid has been omitted from the profile as it was difficult to obtain accurate measurements of velocity in that thin layer by PIV due to light reflections from the rough grid degrading the quality of the images. The far field $\overline{U_\theta}$ is 34 % of the lid velocity at the lowest lid *Re* and 53 % of the lid velocity at the highest lid *Re*. $\overline{U_r}$ is 3–4 times larger inside the bottom boundary layer than in the interior of the fluid column. The turbulent flow between a rotating disk and a stationary disk has been studied experimentally by Itoh *et al.* (1992) and Cheah *et al.* (1994) and numerically using large-eddy simulation (LES) by Andersson & Lygren (2006). Itoh *et al.* (1992) also report the presence of an inner core in which $\overline{U_\theta}$ is homogeneous. Denoting $K = (\overline{U_\theta}/\Omega r)$, they found K in the range

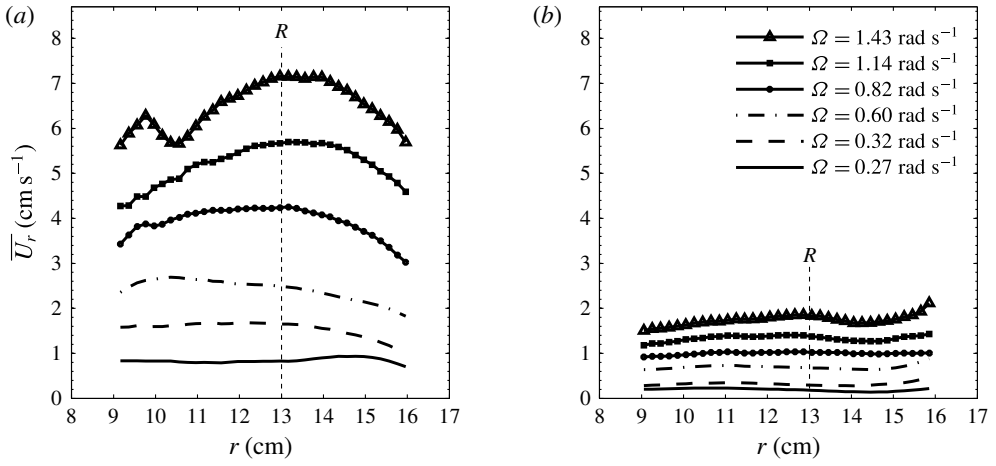

FIGURE 12. Mean radial velocity at heights of (*a*) 0.5 cm and (*b*) 7 cm above the bottom plate. Positive values correspond to inward direction. The vertical dashed line in (*a*) and (*b*) is at $r = R$ where the ice thickness measurements are taken.

31–42 % for local Re ($= \Omega r^2/\nu$) from 1.6×10^5 to 8.8×10^5, which corresponds to 1.3×10^4 to 7.1×10^4 with the definition of Re in (4.1). $\overline{U_r}$ in their experiment was directed inwards in the boundary layer near the stationary plate and was zero in the inner core. In our experiments, the larger values of K at Re one order of magnitude smaller and the non-zero $\overline{U_r}$ in the inner core can be attributed to the roughness of the top boundary, which affects the circulation in the tank by causing enhanced mixing.

4.4. *Friction velocity*

The heat balance in (3.15) also requires knowledge of the friction velocity u_* of the shear-driven flow. Here u_* is defined as

$$u_* = \sqrt{\frac{\tau(\Omega, r)}{\rho}}, \tag{4.5}$$

where τ is the shear stress on the lid, which is given by

$$\tau = C_D \rho_\ell \Omega^2 r^2, \tag{4.6}$$

with C_D being the drag coefficient associated with the lid. Taking dF to be the incremental change in force along an incremental change in radial distance dr from the centre and Γ to be the torque on the lid, Γ and dF are related to C_D by

$$\mathrm{d}F = C_D \rho_\ell \Omega^2 r^2 (2\pi r \,\mathrm{d}r) \tag{4.7}$$

and

$$\Gamma = \int_0^R r \,\mathrm{d}F, \tag{4.8}$$

so that

$$\Gamma = \tfrac{2}{5}\pi C_D \rho_\ell \Omega^2 R^5. \tag{4.9}$$

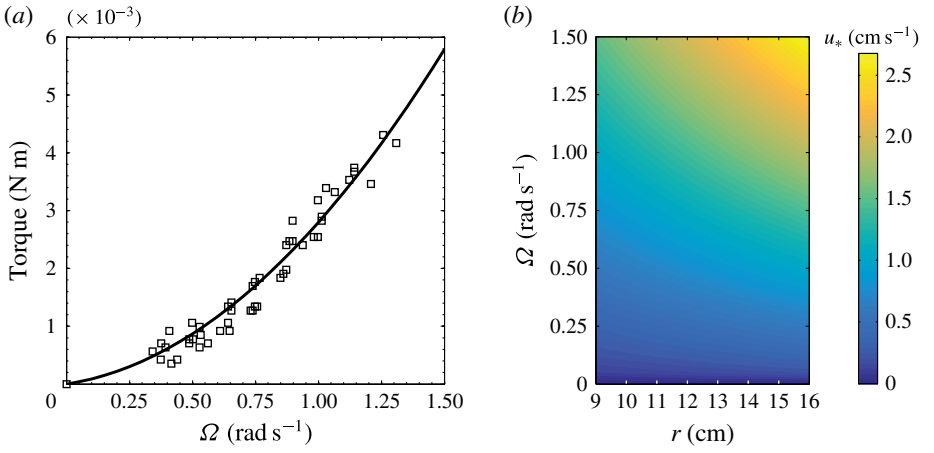

FIGURE 13. (Colour online) (*a*) Torque on the lid for a water depth of 10 cm: □, measurements; ——, line of best fit. (*b*) Friction velocity u_* calculated from torque measurements.

Hence u_* can be determined from Γ according to the relation

$$u_* = \sqrt{\frac{5\Gamma}{2\pi\rho_\ell R^5}}\, r. \tag{4.10}$$

The torque on the lid for different angular velocities of rotation is shown in figure 13(*a*). The line of best fit is a weighted-by-value two-parameter polynomial. The friction velocity derived from the torque measurements using (4.10) is shown in figure 13(*b*).

5. Model comparison

5.1. *Ice thickness*

Our heat balance for the ice–water interface can be integrated in time to model the evolution of ice thickness in the experiments conducted with (3.10) used for Phase 1 and (3.15) used for Phase 2. In what follows, the modelled ice thickness is denoted by h_m. The values listed in table 2 for the properties of liquid water and solid ice are used in the integration. ΔT_s and ΔT_ℓ in the heat balance are calculated in the following way:

$$\Delta T_s = \begin{cases} T_f - T_A, & \text{when ice is present,} \\ 0, & \text{when there is no ice,} \end{cases} \tag{5.1}$$

$$\Delta T_\ell = \begin{cases} T_G - T_f, & \text{when ice is present,} \\ T_G - T_A, & \text{when there is no ice.} \end{cases} \tag{5.2}$$

T_A refers to temperature measurements at thermistor A, which is located in a small hole in the basal cooling plate, and T_G refers to temperature measurements at thermistor G, which is located 5.25 cm above the basal cooling plate. The fluid

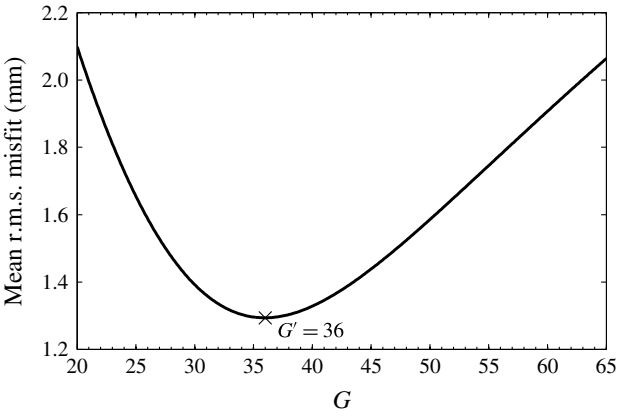

FIGURE 14. Misfit to (3.15) versus G.

velocity in the far field, U_∞, is determined using the measurements of $\overline{U_\theta}$ and $\overline{U_r}$ interpolated at the angular velocity of the lid at a height $z = 7$ cm:

$$U_\infty = \sqrt{\overline{U_\theta(z)}^2 + \overline{U_r(z)}^2}, \quad z = 7 \text{ cm}. \tag{5.3}$$

The friction velocity u_*, which is used in calculating the coefficient of friction c_f defined in (3.14), is determined from the calibration shown in figure 13(*b*). The equations are integrated by a second-order Runge–Kutta method, with the initial condition for h_m being zero. Because the temperature measurements were taken at intervals of 5 s, the time step for integration is also 5 s.

In Phase 2, the heat flux q_T from the turbulent flow at the ice–water interface depends on the coefficient G. For the Pr of water at 0 °C, which is listed in table 1, G becomes 62.7. We denote this value by G_0. The expression for G is an empirical expression derived for a turbulent boundary layer in air over a perfectly flat plate (White 1974). Using a range of values of G, including G_0, we evaluate h_m during Phase 2 of experiments 2–10. We also calculate the root mean square (r.m.s) difference Δh_{RMS} between h_e and h_m at the corresponding times. The omission of experiment 1 from this comparison will be explained when interpreting figure 15(*d*). The mean of Δh_{RMS} for the range of values of G considered is plotted in figure 14. Its minimum occurs when $G = 36.0$. The heat flux from the turbulent layer at the ice–water interface is therefore more closely approximated using this value of G, which will be denoted by G'. The fact that G' is smaller than G_0 indicates that heat transfer from a turbulent flow at an ice–water interface is more efficient than at a flat plate. This enhanced heat transfer can be attributed to the ice surface not being uniformly smooth, especially during melting when it develops a wavy profile, since a rough surface has a greater surface area than a flat surface and hence allows for greater heat transfer. With the new value G', the heat transfer coefficient C_h from the turbulent flow at the ice–water interface given in (3.12) is related to (u_*/U_∞) by the power law $C_h = 0.028(u_*/U_\infty)^{1.09}$.

G' is substituted in (3.15) to calculate h_m for Phase 2 of experiments 1–10. Figure 15 shows the comparison between h_e and h_m in experiments 8, 5, 3 and 1. There is good agreement between h_e and h_m in experiments 8, 5 and 3 but not in Phase 2 of experiment 1. After the onset of turbulent mixing in experiment 1, a

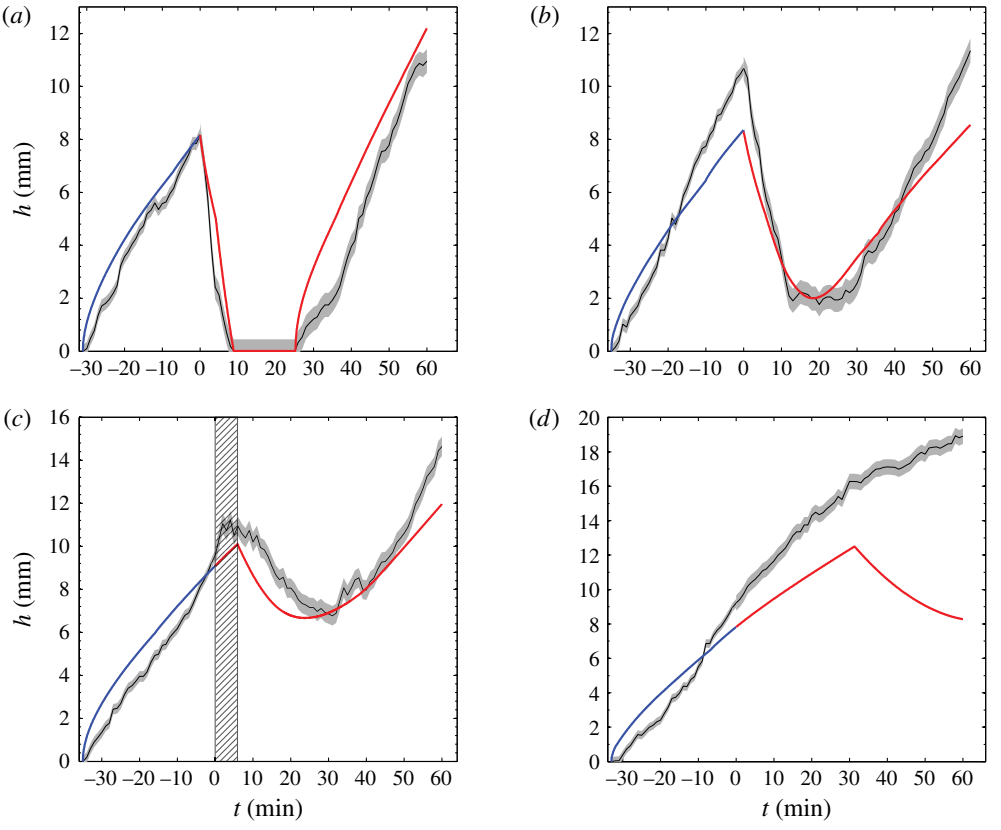

FIGURE 15. (Colour online) Comparison of h_e (thinner solid line with shaded error region) with h_m (thicker solid line) from (*a*) experiment 8, (*b*) experiment 5, (*c*) experiment 3 and (*d*) experiment 1. For $t < 0$, the error in h_e is 0.5 mm and for $t > 0$, it is 0.9 mm. The hatched region in (*c*) is discussed in the text. For the h_m plots, the blue portion corresponds to ice thickness evolution in Phase 1 while the red portion corresponds ice thickness evolution in Phase 2.

stratified layer remained between the turbulent layer and the ice–water interface up to $t = 33$ min. This was evidenced by the behaviour of dye inserted into the turbulent layer, which showed that a clear, stratified layer over the ice–water interface prevented the dyed turbulent layer from reaching the ice surface. Accordingly, the ice growth in that time interval is modelled using (3.10). For this case, the measured rate of ice growth is larger than predicted, a difference which occurs because the stratified layer over the ice–water interface inhibits heat transfer from the liquid far field. Ice grows below the turbulent layer from $t = 0$ to $t = 33$ min, at which time it reaches the turbulence. For $t > 33$ min, h_m is modelled using (3.15). The model predicts melting whereas the experimental measurements indicate attenuated growth. The disagreement between h_e and h_m in experiment 1 reveals a limitation of our model. At the lower end of the range of Re_R we investigate, the applied shear stress from the lid is low, and consequently the turbulence is too weak to erode the stratified layer quickly. Our model, however, assumes that the stratified layer becomes eroded quickly at low values of Re_R.

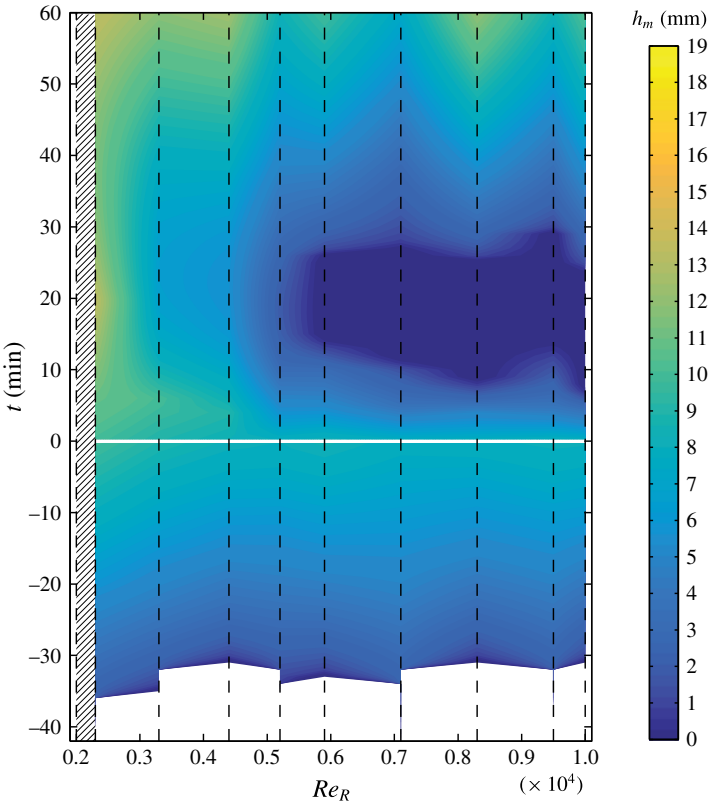

FIGURE 16. (Colour online) Contour plot of h_m for Re_R corresponding to experiments 2–10. The white line represents the onset of turbulent mixing, the dashed vertical black lines indicate the Re_R of the experiments, and the contour plot is filled by linearly interpolating modelled ice thickness values at the distinct Re_R of the experiments.

A stratified layer is present in experiments 2–4 for a short time interval following the onset of turbulent mixing. Although the theoretical model given by (3.10) is incomplete for this configuration, we use it to approximate h_m until the time when the turbulent layer comes into contact with the ice. h_m is consistently lower than h_e in that time interval, as shown in the hatched region of figure 15(*c*) for experiment 3. In the determination of G' previously discussed, h_e and h_m from time intervals when a stratified layer was present were not used.

The contour plot of h_m calculated using the theoretical model with G' for experiments 2–10 is shown in figure 16. Experiment 1 is omitted because it is a case for which our model is not valid. The region corresponding to experiment 1 in figure 16 is hatched. The absolute difference between h_e from figure 5 and h_m at corresponding times is shown in figure 17. The absolute difference is generally close to the error margin of 0.5 mm for Phase 1 and 0.9 mm for Phase 2, which indicates good agreement between the model and the experiment. The hatched area in figure 17 corresponds to experiment 1 and time intervals when a stratified layer was present during Phase 2 of the experiments. The absolute difference between h_e and h_m in these intervals during Phase 2 was omitted from the contour plot because the model assumes that the stratified layer is eroded more rapidly and hence deviates from the experimental measurements.

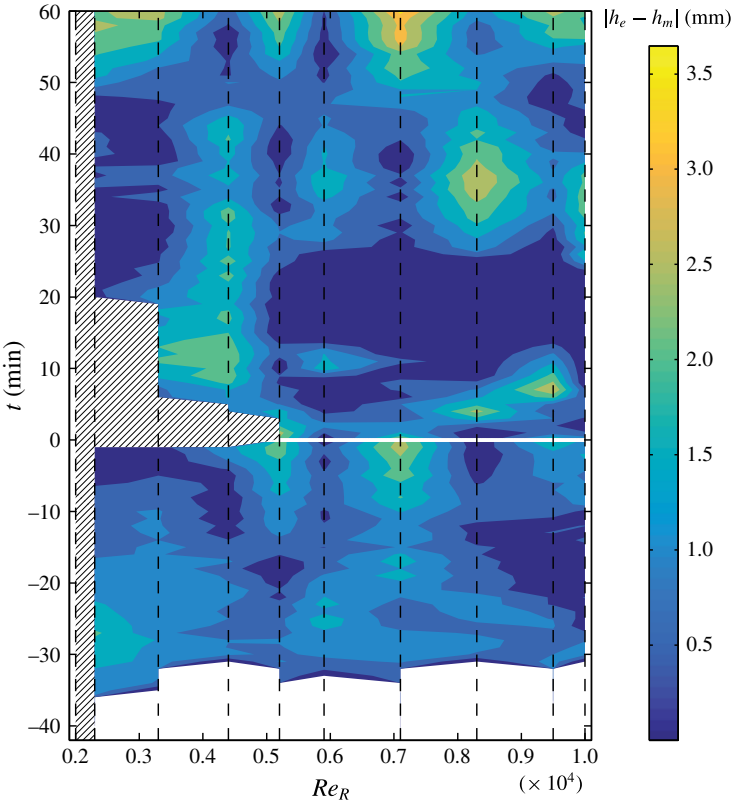

FIGURE 17. (Colour online) Contour plot of absolute difference between h_e and h_m for experiments 2–10. The distinct Re_R of the experiments are marked by the dashed vertical black lines. Data corresponding to the Re_R of the experiments are linearly interpolated to make the contour plot.

We did not observe evidence of the radial component of the flow near the bottom of the tank during turbulent mixing affecting the evolution of ice in our set of experiments. The radial component of the flow is stronger at higher Re_R. In all experiments in which there is transient melting, the rate at which the ice melts always increases with distance from the centre of the tank. During the subsequent refreezing, the rate of ice growth is always uniform at all radial distances. These observations suggest that the far-field flow has a stronger influence on the evolution of ice than the radial flow near the bottom of the tank.

6. Discussion

6.1. *Application to observations under Pine Island Glacier Ice Shelf*

Pine Island Glacier Ice Shelf is a 40 km long, 20 km wide ice shelf in the Amundsen Sea off West Antarctica. An investigation involving the deployment of autonomous underwater vehicles in its underlying ocean cavity showed that the basal surface of the ice shelf is experiencing rapid melting, probably due to shoaling Circumpolar Deep Water and intrusion of warmer water under the ice (Jenkins *et al.* 2010*a*).

Stanton *et al.* (2013) reported *in situ* measurements of the basal melt rate and ocean boundary layer properties from a site in the centre of Pine Island Glacier Ice Shelf

Property	In (3.15)	Units	Value
Ice shelf thickness	h	m	460
Boundary layer density	ρ_ℓ	kg m^{-3}	27.22–27.42
Departure from freezing	ΔT_ℓ	K	1.35–1.42
Mean current velocity	U_∞	m s^{-1}	0.11–0.15
Mean friction velocity	u_*	m s^{-1}	0.0086
Local melting rate	$-\mathrm{d}h/\mathrm{d}t$	m/day	0.039

TABLE 4. Measurements of the ocean boundary layer properties from Stanton *et al.* (2013).

where a hole was drilled vertically from the surface to access the water underneath. We use the measurements, which are listed in table 4, to test our heat transfer model from (3.15) with $G = G'$. The boundary layer depth and density at the site were obtained from conductivity–temperature–depth (CTD) profiling. The departure from freezing, mean current velocity, mean friction velocity and local melting rate were measured using a flux package installed at an initial distance of 2.3 m below the ice shelf base. The range of values listed for the departure from freezing and mean current velocity are for a 35 day period. The mean friction velocity was constant in that period. The local melt rate is from a fit through measurements from days 5–35 and is equivalent to 14 m yr^{-1}. We substitute h, u_*, and the medians of the range of values of ρ_ℓ, ΔT_ℓ and U_∞ from table 4, ρ_s, k_s and L from table 2, a typical value of $c_\ell = 4.00 \times 10^3$ J kg^{-1} K^{-1} for sea water and a typical value of $\Delta T_s = 19$ K (Tyler *et al.* 2013) for an Antarctic ice shelf in (3.15). This yields a predicted melt rate $-\mathrm{d}h/\mathrm{d}t$ of 98 m yr^{-1}.

The fact that our model over-predicts the observed melt rate can be partly explained by the observed ΔT_ℓ being across a thick stable stratified boundary layer. Our model is not valid for the interaction of a stable stratified layer with an ice–water interface. Eddy diffusivity in a stratified turbulent flow is lower than in an unstratified turbulent flow (Galperin, Sukoriansky & Anderson 2007), which can account partly for the discrepancy between the observed and modelled melt rates. Our predicted value of the melt rate at the measurement site is an upper limit and corresponds to the case where a well-mixed turbulent warm water flow comes in direct contact with the ice–water interface.

In this application, phase change due to heat transfer through the boundary layer only is considered. The transfer of salt through the boundary layer is ignored. A mean vertical salt flux of 2.8×10^{-6} psu ms^{-1} was also measured at the observation site by Stanton *et al.* (2013). Both the conservation of heat and the conservation of salt at the interface control the rate of phase change. Whether heat transfer or salt transfer is the more dominant effect in causing the phase change at this site remains an open question. A complete analysis should consider both effects, and include data from different levels within the boundary layer.

6.2. *Comparison of γ_T from our model with other expressions for γ_T*

The parameterization of the thermal exchange velocity across the boundary layer in our model is

$$\gamma_T = U_\infty C_h = U_\infty \left(\frac{c_f/2}{1 + G'\sqrt{c_f/2}} \right). \tag{6.1}$$

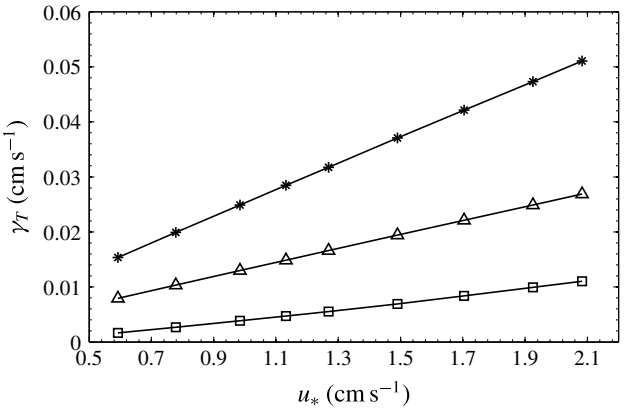

FIGURE 18. Thermal exchange velocity γ_T corresponding to the u_* from our experiments: $*$ from (6.1), $\triangle$ from (6.2) and $\square$ from Jenkins (2011).

This parameterization is compared against two formulations used in the literature. Jenkins (1991) expressed γ_T as

$$\gamma_T = \frac{C_d^{1/2} U_\infty}{2.12 \ln(C_d^{1/2} Re) + 12.5 Pr^{2/3} - 8.68}, \tag{6.2}$$

where C_d is a dimensionless drag coefficient given by

$$C_d = \frac{u_*^2}{U_\infty^2}. \tag{6.3}$$

The expressions (6.1) and (6.2) for γ_T are essentially equivalent, being related by the Prandtl–Nikuradse skin friction law (Kader & Yaglom 1972). A constant Stanton number C_h is used by Jenkins (2011) for heat transfer through the boundary layer. This is converted to the thermal exchange velocity γ_T using $\gamma_T = U_\infty C_h$. The values of γ_T calculated from (6.1), (6.2) and the constant Stanton number of Jenkins (2011) for the range of friction velocities covered by experiment 2–10 are compared in figure 18. For the configuration where a warm turbulent layer is in direct contact with an ice surface, our experimentally constrained model estimates that the thermal exchange velocity is larger than conventional models assume.

7. Summary

We have conducted experiments on the melting of ice in a turbulent shear flow that transports warm water to the ice–water interface. A modified heat transfer law, originally derived for turbulent flow over a flat plate and which depends on the friction velocity of the flow, allows us to model the evolution of the ice thickness correctly. Our experiments have dynamic similarity with the geophysical system of the ocean cavity beneath an ice shelf through the Rossby number and thermodynamic similarity through the Stefan number. Although our experiments do not include the effect of salinity, they reveal the mechanisms through which warm water transport to an ice shelf's basal surface accelerates basal melting. Through this study, we propose an experimentally constrained expression for the thermal exchange velocity γ_T in ice–ocean interaction.

Acknowledgements

We thank Y. Li and H. Chen for help in conducting the PIV measurements. We also thank X. I. A. Yang for helpful discussion. The experiments were financially supported by NSF grant EAR-110371.

REFERENCES

ANDERSSON, H. I & LYGREN, M. 2006 LES of open rotor–stator flow. *Intl J. Heat Fluid Flow* **27** (4), 551–557.

BOGER, D. V. & WESTWATER, J. W. 1967 Effect of buoyancy on the melting and freezing process. *Trans. ASME J. Heat Transfer* **89** (1), 81–89.

BRISBOURNE, A. M., SMITH, A. M., KING, E. C., NICHOLLS, K. W., HOLLAND, P. R. & MAKINSON, K. 2014 Seabed topography beneath Larsen C Ice Shelf from seismic soundings. *Cryosphere* **8**, 1–13.

BROECKER, W. S., PEACOCK, S. L., WALKER, S., WEISS, R., FAHRBACH, E., SCHRÖDER, M., MIKOLAJEWICZ, U., HEINZE, C., KEY, R., PENG, T.-H. *et al.* 1998 How much deep water is formed in the Southern Ocean? *J. Geophys. Res.* **103** (C8), 15833–15843.

CHEAH, S. C., IACOVIDES, H., JACKSON, D. C., JI, H. & LAUNDER, B. E. 1994 Experimental investigation of enclosed rotor-stator disk flows. *Exp. Therm. Fluid Sci.* **9** (4), 445–455.

DALLASTON, M. C., HEWITT, I. J. & WELLS, A. J. 2015 Channelization of plumes beneath ice shelves. *J. Fluid Mech.* **785**, 109–134.

DANSEREAU, V., HEIMBACH, P. & LOSCH, M. 2014 Simulation of subice shelf melt rates in a general circulation model: velocity-dependent transfer and the role of friction. *J. Geophys. Res. Oceans* **119**, 1765–1790.

FELDMANN, J. & LEVERMANN, A. 2015 Collapse of the West Antarctic Ice Sheet after local destabilization of the Amundsen Basin. *Proc. Natl Acad. Sci. USA* **112**, 14191–14196.

GALPERIN, B., SUKORIANSKY, S. & ANDERSON, P. S. 2007 On the critical Richardson number in stably stratified turbulence. *Atmos. Sci. Lett.* **8** (3), 65–69.

GILPIN, R. R., HIRATA, T. & CHENG, K. C. 1980 Wave formation and heat transfer at an ice–water interface in the presence of a turbulent flow. *J. Fluid Mech.* **99**, 619–640.

HAYNES, W. M. 2015 *CRC Handbook of Chemistry and Physics: A Ready-Reference Book of Chemical and Physical Data*. CRC.

HELLMER, H. H. & OLBERS, D. J. 1989 A two-dimensional model for the thermohaline circulation under an ice shelf. *Antarct. Sci.* **1** (4), 325–336.

HOLLAND, D. M. & JENKINS, A. 1999 Modeling thermodynamic ice-ocean interactions at the base of an ice shelf. *J. Phys. Oceanogr.* **29** (8), 1787–1800.

HOLLAND, P. R. & FELTHAM, D. L. 2006 The effects of rotation and ice shelf topography on frazil-laden ice shelf water plumes. *J. Phys. Oceanogr.* **36** (12), 2312–2327.

HOOKE, R. L. 2005 *Principles of Glacier Mechanics*. Cambridge University Press.

HUPPERT, H. E. & WORSTER, M. G. 1985 Dynamic solidification of a binary melt. *Nature* **314**, 703–707.

IOC, SCOR & IAPSO 2010 *The International Thermodynamic Equation of Seawater – 2010: Calculation and Use of Thermodynamic Properties*. Intergovernmental Oceanographic Commission, Manuals and Guides No. 56, UNESCO (English).

ITOH, M., YAMADA, Y., IMAO, S. & GONDA, M. 1992 Experiments on turbulent flow due to an enclosed rotating disk. *Exp. Therm. Fluid Sci.* **5** (3), 359–368.

JACOBS, S. S., JENKINS, A., GIULIVI, C. F. & DUTRIEUX, P. 2011 Stronger ocean circulation and increased melting under Pine Island Glacier ice shelf. *Nat. Geosci.* **4**, 519–523.

JENKINS, A. 1991 A one-dimensional model of ice shelf-ocean interaction. *J. Geophys. Res. Oceans* **96** (C11), 20671–20677.

JENKINS, A. 2011 Convection-Driven Melting near the Grounding Lines of Ice Shelves and Tidewater Glaciers. *J. Phys. Oceanogr.* **41** (12), 2279–2294.

JENKINS, A., DUTRIEUX, P., JACOBS, S. S., MCPHAIL, S. D., PERRETT, J. R., WEBB, A. T. & WHITE, D. 2010*a* Observations beneath Pine Island Glacier in West Antarctica and implications for its retreat. *Nat. Geosci.* **3**, 468–472.

JENKINS, A., NICHOLLS, K. W. & CORR, H. F. J. 2010*b* Observation and parameterization of ablation at the base of Ronne Ice Shelf, Antarctica. *J. Phys. Oceanogr.* **40** (10), 2298–2312.

KADER, B. A. & YAGLOM, A. M. 1972 Heat and mass transfer laws for fully turbulent wall flows. *Intl J. Heat Mass Transfer* **15**, 2329–2351.

KERR, R. C. & MCCONNOCHIE, C. D. 2015 Dissolution of a vertical solid surface by turbulent compositional convection. *J. Fluid Mech.* **765**, 211–228.

LITTLE, C. M., GNANADESIKAN, A. & HALLBERG, R. 2008 Large-scale oceanographic constraints on the distribution of melting and freezing under ice shelves. *J. Phys. Oceanogr.* **38** (10), 2242–2255.

MARINOV, I., GNANADESIKAN, A., SARMIENTO, J. L., TOGGWEILER, J. R., FOLLOWS, M. & MIGNONE, B. K. 2008 Impact of oceanic circulation on biological carbon storage in the ocean and atmospheric pCO2. *Glob. Biogeochem. Cycles* **22** (3), GB3007.

MCPHEE, M. G., MAYKUT, G. A. & MORISON, J. H. 1987 Dynamics and thermodynamics of the ice/upper ocean system in the marginal ice zone of the greenland sea. *J. Geophys. Res. Oceans* **92** (C7), 7017–7031.

MUELLER, R. D., PADMAN, L., DINNIMAN, M. S., EROFEEVA, S. Y., FRICKER, H. A. & KING, M. A. 2012 Impact of tide-topography interactions on basal melting of Larsen C Ice Shelf, Antarctica. *J. Geophys. Res. Oceans* **117** (C5), C05005.

NEUFELD, J. A. & WETTLAUFER, J. S. 2008 An experimental study of shear-enhanced convection in a mushy layer. *J. Fluid Mech.* **612**, 363–385.

PRITCHARD, H. D., LIGTENBERG, S. R. M., FRICKER, H. A., VAUGHAN, D. G., VAN DEN BROEKE, M. R. & PADMAN, L. 2012 Antarctic ice-sheet loss driven by basal melting of ice shelves. *Nature* **484**, 502–505.

SCHEDUIKAT, M. & OLBERS, D. J. 1990 A one-dimensional mixed layer model beneath the Ross Ice Shelf with tidally induced vertical mixing. *Antarc. Sci.* **2** (1), 29–42.

SCHMIDTKO, S., HEYWOOD, K. J., THOMPSON, A. F. & AOKI, S. 2014 Multidecadal warming of Antarctic waters. *Science* **346**, 1227–1231.

STANTON, T. P., SHAW, W. J., TRUFFER, M., CORR, H. F. J., PETERS, L. E., RIVERMAN, K. L., BINDSCHADLER, R., HOLLAND, D. M. & ANANDAKRISHNAN, S. 2013 Channelized ice melting in the ocean boundary layer beneath Pine Island Glacier, Antarctica. *Science* **341**, 1236–1239.

STERN, A. A., HOLLAND, D. M., HOLLAND, P. R., JENKINS, A. & SOMMERIA, J. 2014 The effect of geometry on ice shelf ocean cavity ventilation: a laboratory experiment. *Exp. Fluids* **55** (5), 1–19.

THIELICKE, W. & STAMHUIS, E. J. 2014 PIVlab – towards user-friendly, affordable and accurate digital particle image velocimetry in matlab. *J. Open Res. Software* **2** (1), e30.

TOWNSEND, A. A. 1964 Natural convection in water over an ice surface. *Q. J. R. Meteorol. Soc.* **90** (385), 248–259.

TYLER, S. W., HOLLAND, D. M., ZAGORODNOV, V., STERN, A. A., SLADEK, C., KOBS, S., WHITE, S., SUÁREZ, F. & BRYENTON, J. 2013 Using distributed temperature sensors to monitor an Antarctic ice shelf and sub-ice-shelf cavity. *J. Glaciol.* **59** (215), 583–591.

WAGNER, W. & PRUSS, A. 2002 The IAPWS formulation 1995 for the thermodynamic properties of ordinary water substance for general and scientific use. *J. Phys. Chem. Ref. Data* **31** (2), 387–535.

WELLS, A. J. & WORSTER, M. G. 2011 Melting and dissolving of a vertical solid surface with laminar compositional convection. *J. Fluid Mech.* **687**, 118–140.

WETTLAUFER, J. S., WORSTER, M. G. & HUPPERT, H. E. 1997 Natural convection during solidification of an alloy from above with application to the evolution of sea ice. *J. Fluid Mech.* **344**, 291–316.

WHITE, F. M. 1974 *Viscous Fluid Flow*. McGraw-Hill.

YAGLOM, A. M. & KADER, B. A. 1974 Heat and mass transfer between a rough wall and turbulent fluid flow at high Reynolds and Peclet numbers. *J. Fluid Mech.* **62**, 601–623.